Journal of Geodesy (2025) 99:4
https://doi.org/10.1007/s00190-024-01922-6

ORIGINAL ARTICLE

Finite volume method: a good match to airborne gravimetry?

Xiaopeng Li[1] · Robert Čunderlík[2] · Marek Macák[2] · Dana J. Caccamise II[3] · Zuzana Minarechová[2] · Pavol Zahorec[4] · Juraj Papčo[2] · Daniel R. Roman[5] · Jordan Krcmaric[1] · Miao Lin[6]

Received: 5 March 2024 / Accepted: 14 November 2024

Abstract
Numerical methods, like the finite element method (FEM) or finite volume method (FVM), are widely used to provide solutions in many boundary value problems. In previous studies, these numerical methods have also been applied in geodesy but demanded extensive computations because the upper boundary condition was usually set up at the satellite orbit level, hundreds of kilometers above the Earth. The relatively large distances between the lower boundary of the Earth's surface and the upper boundary exacerbate the computation loads because of the required discretization in between. Considering that many areas, such as the US, have uniformly distributed airborne gravity data just a few kilometers above the topography, we adapt the upper boundary from the satellite orbit level to the mean flight level of the airborne gravimetry. The significant decrease in the domain of solution dramatically reduces the large computation demand for FEM or FVM. This paper demonstrates the advantages of using FVM in the decreased domain in simulated and actual field cases in study areas of interest. In the simulated case, the FVM numerical results show that precision improvement of about an order of magnitude can be obtained when moving the upper boundary from 250 to 10 km, the upper altitude of the GRAV-D flights. A 2–3 cm level of accurate quasi-geoid model can be obtained for the actual datasets depending on different schemes used to model the topographic mass. In flat areas, the FVM solution can reach to about 1 cm precision, which is comparable with the counterparts from classical methods. The paper also demonstrates how to find the upper boundary if no airborne data are available. Finally, the numerical method provides a 3D discrete representation of the entire local gravity field instead of a surface solution, a (quasi) geoid model.

Keywords Airborne gravimetry · Finite volume method · Geoid modeling · Quasi-geoid computation

1 Introduction

The geodetic boundary value problem (GBVP) starts with the Laplace equation and the boundary condition (BC) on the geoid. Traditionally, the solution can be derived by using Green's identities (Heiskanen and Moritz 1967). Stokes-Helmert's or Molodenski's method is typically used in local gravity field modeling, which yields the geoid or quasi-geoid models. A general description of their implementations can be found in numerous local geoid modeling papers, such as the recent Colorado test summary paper (Wang et al. 2021). For more detailed information on the specifics of the implementation of Stokes–Helmert's method, we recommend Huang and Véronneau (2013) as a starting point simply because their implementation schemes yielded the best solution in the recent Colorado test. Molodenski's method is exemplified in Denker et al. (2009), while Sjöberg and Abrehdary (2023) offer insightful remarks on determining geoid

✉ Xiaopeng Li
Xiaopeng.Li@noaa.gov

1 Geosciences Research Division, National Geodetic Survey, 1315 East-West Highway, Silver Spring, MD 20910, USA

2 Faculty of Civil Engineering, Slovak University of Technology, Radlinskeho 11, 810 05 Bratislava, Slovakia

3 MC 0225 GPP Revelle - 3206, Scripps Institution of Oceanography, UCSD, 8775 Biological Grade, La Jolla, CA 92037, USA

4 Department of Gravimetry and Geodynamics, Earth Science Institute, Slovak Academy of Sciences, Ďumbierska 1, 974 01 Banská Bystrica, Slovakia

5 National Geodetic Survey, Silver Spring, MD 20910, USA

6 College of Civil Engineering, Xiangtan University, Xiangtan 411105, China

Published online: 18 December 2024

and quasi-geoid separations. In addition to these classical methods, relatively recently, the spherical radial basis functions (SRBF) method has been also used in local geoid and quasi-geoid modeling (Schmidt et al. 2007; Klees et al. 2008). However, it heavily relies on regularization, especially when airborne gravimetric data are involved (Li 2018b). Other methods, such as least-squares collocation (LSC, Tscherning and Rapp 1974, and Moritz 1980), can also be used. However, these "analytical" solutions must grapple with the unfathomable difficulties in the downward continuation step (Li et al. 2022). Hence, numerical methods without explicitly dealing with the radial ratio term ($(\frac{R}{r})^{n+1}$) will be desirable to simplify the problem.

The finite element method (FEM) (Reddy 2006) and finite volume method (FVM) (Eymard et al. 2000) are widely used to solve boundary value problems (BVPs) where analytical solutions are either too complex to obtain or do not exist. Their applications have gained momentum in geodesy, especially in recent years when high-performance computing (HPC) systems become more accessible (see, e.g., Fašková et al. 2010; Minarechová et al. 2015, 2021; Macák et al. 2021; Čunderlík et al. 2020, 2024). The number of discretization elements largely depends on the upper and lower boundary distances. The upper boundary is often set at the altitude of the satellite orbit level to exploit their in situ observations. Thus, the resulting domain to be solved vertically spans about 250 km. This demands colossal computation efforts, especially for high-resolution and high-accuracy models.

Airborne gravimetry has been used for decades (Childers et al. 1999; Forsberg et al. 2001; Li 2011). Uniformly distributed airborne gravity data coverage in many regions is not uncommon these days. Moreover, they are registered just a few kilometers above the local topography and significantly improve the precision of the local models (Li et al. 2016). Thus, the upper boundary in the FEM or FVM approaches can be easily shifted down from the satellite orbit level to the flight altitudes. The use of airborne gravity data significantly reduces the large computation requirements in the FEM or FVM applications. This is the primary motivation of this study, which is focused on the application of the FVM approach for airborne gravity data.

The rest of the paper is organized in the following way. Section 2 describes a brief mathematical background of FVM for solving GBVP numerically. Section 3 demonstrates some typical numerical behaviors of the FVM using simulated synthetic data to highlight the effects of changing altitudes of the upper boundary. Section 4 uses real datasets to generate a local quasi-geoid model in the study area in Colorado, USA, which is a mountainous area. The results are evaluated using the recent GNSS/Leveling dataset collected by the Geoid Slope Validation Survey of 2017 (Van Westrum et al. 2021 and Wang et al. 2021), which is one of the most accurate validation datasets in the world, as historical GNSS/Leveling datasets are often subject to systematic errors or various natural motions (see e.g., Li 2018a). The $\text{FVM}_{\text{GRAV-D}}$ scheme is also tested in a flat area, Southern Texas, which also has accurate GNSS/Leveling benchmarks (Smith et al. 2013). For both of the testing areas, the solutions are compared with their counterparts from the classical method head-to-head. Finally, discussions are given in Sect. 5, and summary is made in Sect. 6.

2 FVM as a numerical method to solve GBVP

In classical GBVP, the analytical solution of the disturbing potential T is given by:

$$\begin{aligned} T(r,\theta,\lambda) &= \frac{R}{4\pi}\iint_{\sigma}\Delta g\sum_{n=2}^{\infty}\left(\frac{2n+1}{n-1}\left(\frac{R}{r}\right)^{n+1}\right)P_n(cos\psi)d\sigma \\ &= \frac{R}{4\pi}\iint_{\sigma}S(r,\psi)\Delta g d\sigma \overset{on\ the\ geoid}{\Longrightarrow} T(R,\theta,\lambda) \\ &= \frac{R}{4\pi}\iint_{\sigma}S(\psi)\Delta g d\sigma \end{aligned} \tag{1}$$

where $r=\sqrt{x^2+y^2+z^2}$ is the radial distance of the computation point with Cartesian coordinate (x, y, z), θ and λ are the co-latitude and longitude, R is the mean radius of the Earth, ψ is the angle between the computation point and the integration point, P_n is the Legendre's polynomials of degree n, Δg is a global gravity anomaly grid on the bounding sphere, $\iint_{\sigma}$ denotes the usual abbreviation for an integral extended over the full solid angle, and $d\sigma$ is the element of solid angle (Heiskanen and Moritz 1967). The kernel function $S(r, \psi)$ is given by Eq. (2).

$$\begin{aligned} S(r,\psi) = &\frac{2R}{l}+\frac{R}{r}-3\frac{Rl}{r^2} \\ &-\frac{R^2}{r^2}cos\psi\left(5+3ln\frac{r-Rcos\psi+l}{2r}\right). \end{aligned} \tag{2}$$

When $R=r$, it reduces to

$$\begin{aligned} S(\psi) = S(R=r,\psi) = &\frac{1}{\sin(\psi/2)}-6sin\frac{\psi}{2}+1 \\ &-5cos\psi-3cos\psi ln\left(sin\frac{\psi}{2}+sin^2\frac{\psi}{2}\right), \end{aligned} \tag{3}$$

where

$$l=\sqrt{r^2+R^2-2Rrcos\psi}. \tag{4}$$

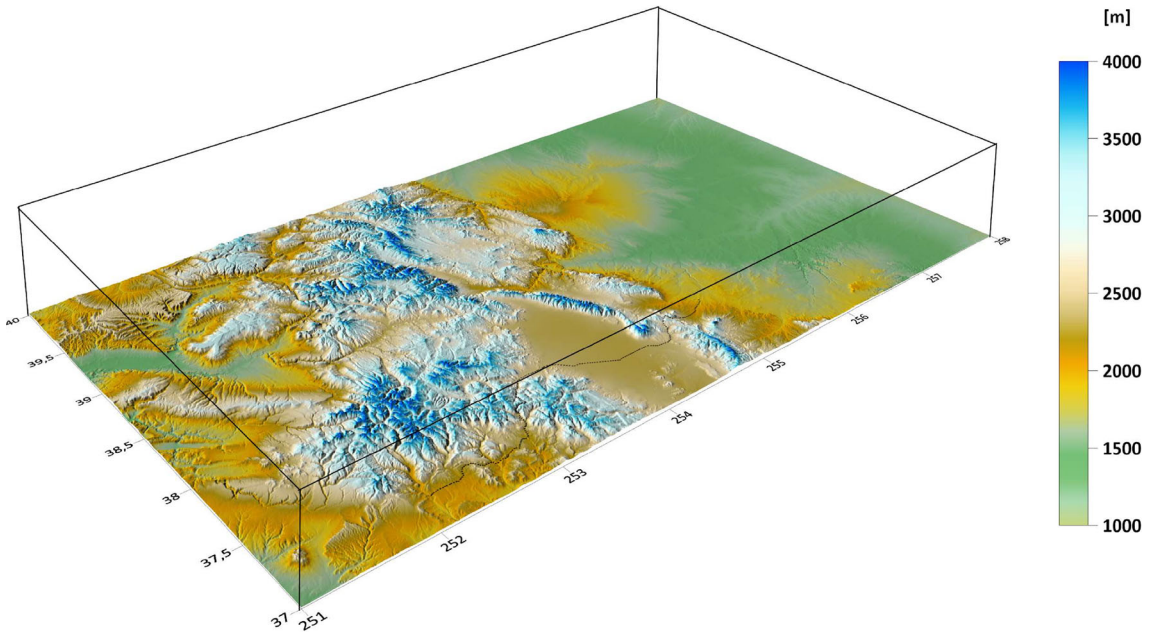

Fig. 1 A sketch of the 3D computational domain of the FVM approach for local gravity field modeling

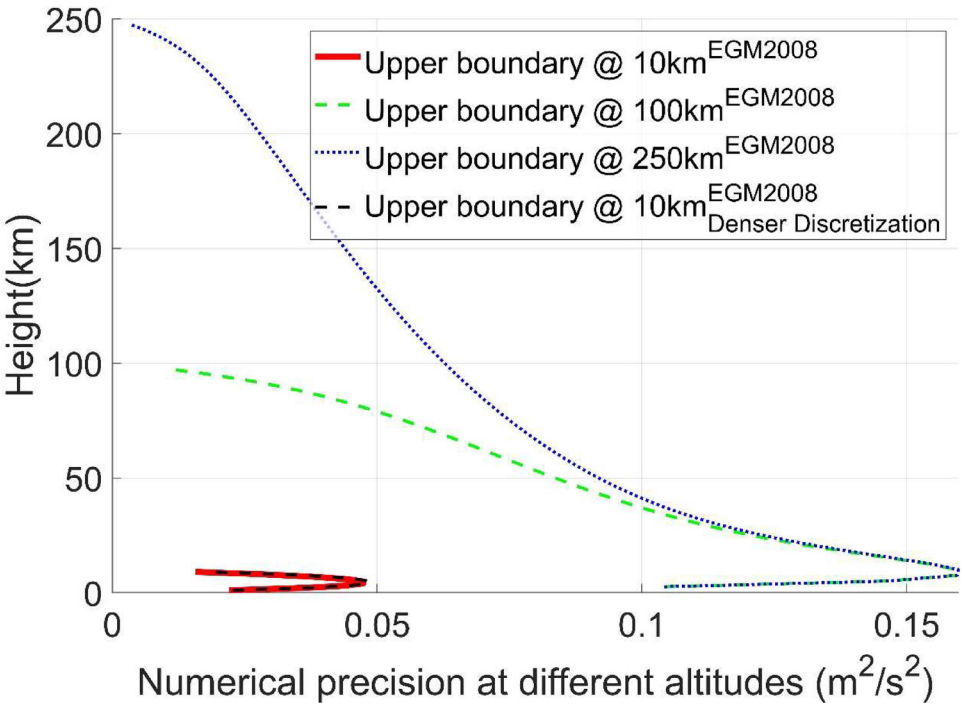

Fig. 2 The root mean squared errors, the differences between the FVM modeled disturbing potential and the true values, at different layers when using different upper BCs synthesized from the full field EGM2008 (complete to d/o 2190) at different altitudes (250 km indicated by the blue dotted curve, 100 km described by green dashed curve and 10 km represented by the thick red curve, respectively)

To compute a geoid model or a quasi-geoid model, all gravity data need to be downward continued (Li et al. 2022) onto the geoid or a level surface, respectively. And the kernel function, $S(\psi)$, has to be modified to minimize the far zone contribution effects, since the integration is usually limited in a local area (Li and Wang 2011).

Unlike the classical approach, FVM is a numerical method of variational calculus, where the first step is a division of the whole computational domain into finite volumes p. The shape of these volumes can be various, but for our needs we consider the spherical prisms (Minarechová et al. 2015). To obtain a weak formulation of the Laplace equation for the disturbing potential T, this governing equation is integrated over the finite volume p using the divergence theorem. In this way, we convert the volume integral, $\iiint dv$, to the surface integral, $\iint ds$, with the normal derivative of the disturbing

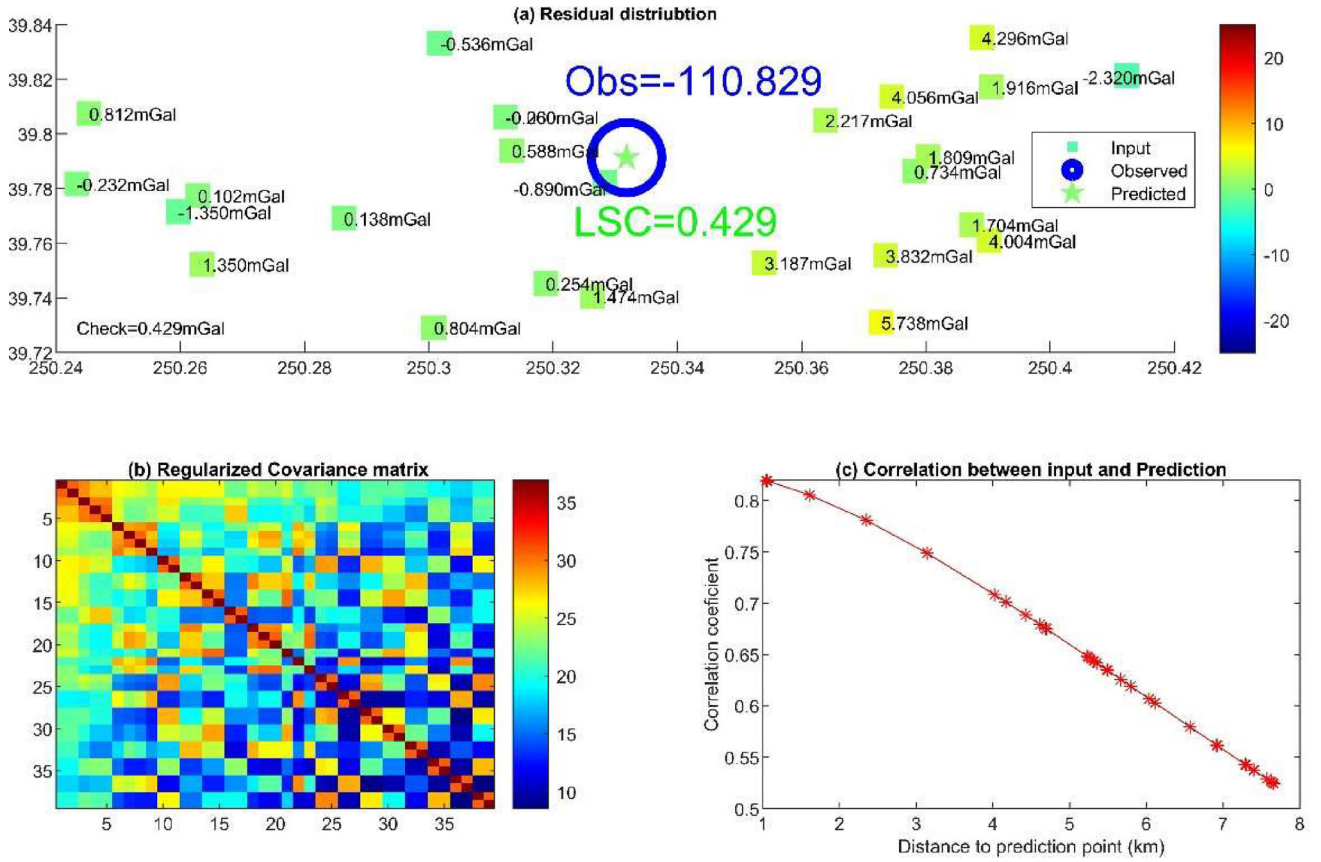

Fig. 3 Example of the RTM-based data cleaning algorithm applied in the target area (The upper panel (**a**) shows the location of the points, indicated by the small squares, near to the point under investigation, the blue circle (the 13,740th point in the published dataset). The lower left panel (**b**) shows the regularized covariance matrix used in LSC. The lower right panel (**c**) shows the correlation coefficient between the input data and the predicted value—indicated by the asterisk dashed red curve (should be gradually decreasing with increase in the distance)

potential $\frac{\partial T}{\partial n}$, namely,

$$-\iiint_p \Delta T d\mathrm{x}\mathrm{d}y\mathrm{d}z = -\sum_{q\in N(p)} \iint_{e_{pq}} \nabla T \cdot \vec{n}\mathrm{d}\sigma$$
$$= -\sum_{q\in N(p)} \iint_{e_{pq}} \frac{\partial T}{\partial n}\mathrm{d}\sigma = 0, \quad (5)$$

where $N(p)$ denotes all direct neighbors of the finite volume p and e_{pq} is a boundary of the finite volume p common with its neighboring finite volume q, $\vec{n}$ is the unit outer normal to the boundary e_{pq}. To obtain the FVM numerical scheme, the normal derivative is approximated by $\frac{\partial T}{\partial n} \approx \frac{T_q - T_p}{d_{pq}}$ and $\mathrm{d}\sigma = m_{pq}$, where m_{pq} is the area of e_{pq} and d_{pq} denotes the distance between the centers of finite volumes p and q. In this way, the following equation is established for every finite element p.

$$-\sum_{q\in N_p} \frac{T_q - T_p}{d_{pq}} m\left(e_{pq}\right) = \sum_{q\in N_p} \frac{m\left(e_{pq}\right)}{d_{pq}} \left(T_p - T_q\right)$$
$$= 0, \quad (6)$$

where $\frac{m(e_{pq})}{d_{pq}}$ is referred to as a transmissivity coefficient (Eymard et al. 2000). By denoting these transmissivity coefficients in the cardinal directions, we obtain the linear system of equations that can be written in the form

$$P_{i,j,k}T_{i,j,k} - W_{i,j,k}T_{i-1,j,k} - E_{i,j,k}T_{i+1,j,k}$$
$$- N_{i,j,k}T_{i,j+1,k} - S_{i,j,k}T_{i,j-1,k}$$
$$- U_{i,j,k}T_{i,j,k+1} - D_{i,j,k}T_{i,j,k-1} = 0, \quad (7)$$

where W, E, N, S, U, D are the transmissivity coefficients on the "west, east, north, south, up and down" sides of the finite volumes p, while $i = 1, \ldots, n_1$, $j = 1 \ldots n_2$, $k = 1 \ldots n_3$ and n_1, n_2 and n_3 stand for the number of divisions in the longitudinal, latitudinal and height directions,

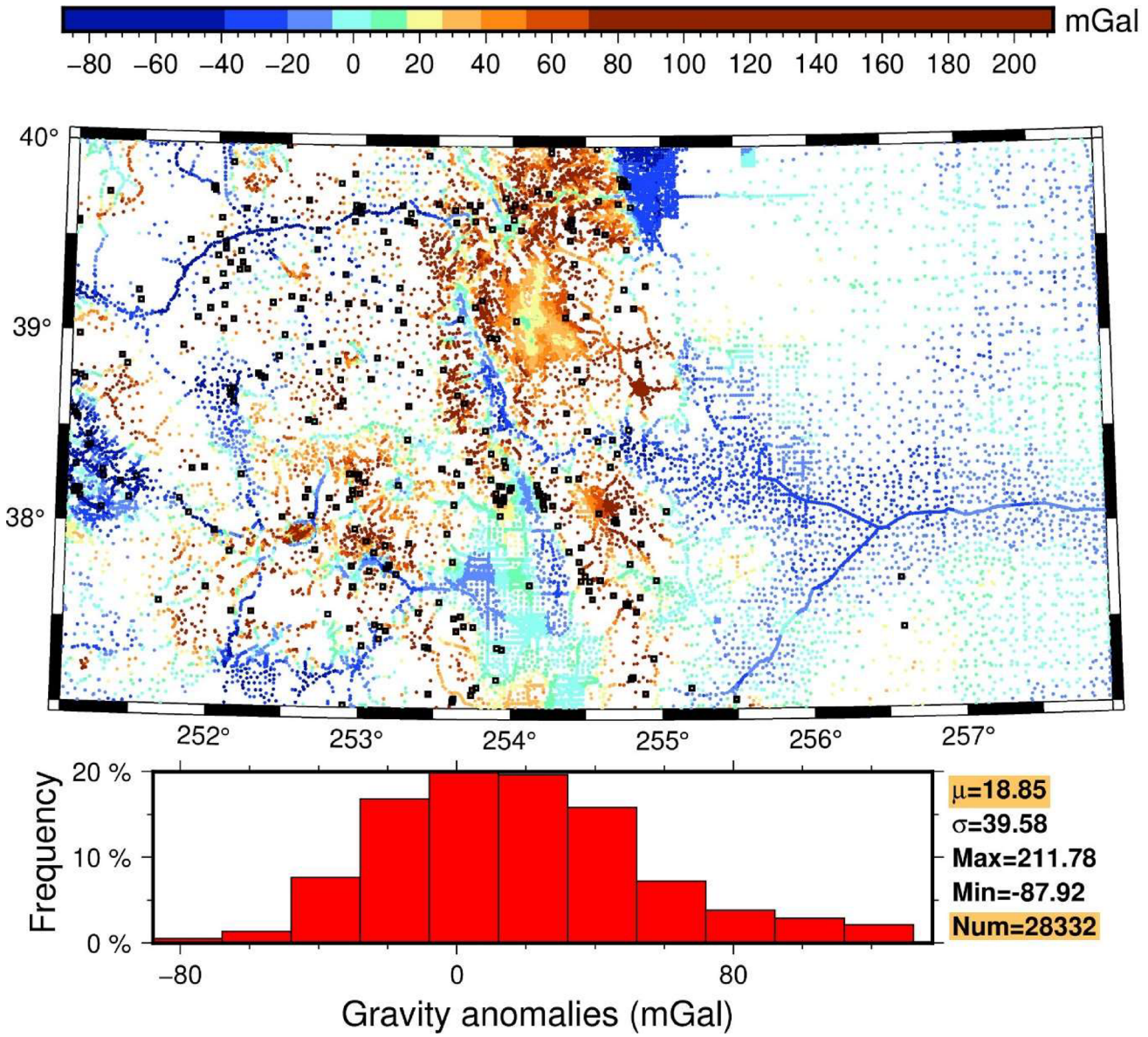

Fig. 4 The cleaned data point in the target area (Deleted points are indicated by the black squares. The histogram shows the gravity anomalies that are normally distributed with a no zero mean value, ~ 19 mGal, and a rather large standard deviation, ~ 40 mGal)

respectively. The diagonal coefficient P is obtained from the relation

$$P_{i,j,k} = W_{i,j,k} + E_{i,j,k} + N_{i,j,k} + S_{i,j,k} + U_{i,j,k} + D_{i,j,k}. \tag{8}$$

The exact formulas of how to calculate the transmissivity coefficients W, E, N, S, U, D are derived in Minarechová et al. (2015).

Before solving this linear system of equations, the boundary conditions (BCs) have to be taken into account. In case disturbing potential T is directly prescribed on the corresponding boundary. In case of the Neumann BC, the gravity disturbance, δg is prescribed. Afterward, the linear system of equations can be solved, which results in the disturbing potential obtained in the whole 3D computational domain.

The input gravity disturbances implemented on the bottom boundary as the Neumann BC (Fig. 1) directly correspond to the fluxes. This benefit is one of the reasons why it is natural to apply the FVM to the solution of the BVPs with the Laplace equation and the Neumann BC. In general, the FVM is a conservative method because the flux entering a given volume is identical to that leaving the adjacent volume. Another advantage of the FVM is its ability to accommodate unstructured meshes, making it particularly appealing for computational fluid dynamics. More details about solving the GBVP with the Neumann BC can be found in Minarechová et al. (2015).

Table 1 Summary of the statistics of values in Figs. 4, 5, 6, 7, 8 and 11a

Figures	Mean	SD	Min	Max	Quantity (units)
4	18.85	39.58	− 87.92	211.78	Δg (mGal)
5	− 5.10	17.08	− 111.05	82.60	$\delta g - \delta g_{2190}^{XGgeoid22refA}$ (mGal)
6	1.93	5.81	− 38.56	37.06	$\delta g - \delta g_{2190}^{XGgeoid22refA} - \delta g^{RTM}$ (mGal)
7	− 253.971	42.93	− 340.47	− 126.38	Δg^{CBA} (mGal)
8a	12.95	43.84	− 100.89	316.80	δg (mGal)
8b	12.03	40.71	− 102.63	203.51	δg (mGal)
8c	12.69	40.40	− 92.95	202.89	δg (mGal)
8d	12.92	38.61	− 81.66	158.80	δg (mGal)
11a	0.00	0.00	− 0.01	0.01	$T_{EGM2008}^{2190} - T_{EGM2008}^{360}$ (m^2/s^2)

3 Numerical tests of FVM to reconstruct EGM2008

In this section, simulated data synthesized from EGM2008 (Pavlis et al. 2012) demonstrate the effects when the upper boundary is set at different altitudes. The full model (up to degree and order (d/o) 2190) is used at various boundaries to illustrate the effects of the placements of the upper boundary on the final solution. The selected study area is in the Colorado testing bed (Wang et al. 2021), with latitude ranges from 37 degrees North to 40 degrees North; longitude ranges from 251 to 258 degrees. On the bottom boundary of the 3D computational domain (Fig. 1), the surface gravity disturbances are prescribed. From the mathematical point of view, they represent the oblique derivative BC; however, for structured meshes they can be simplified into the Neumann BC (Minarechová et al. 2015). On the rest of the domain boundary, the disturbing potential as the Dirichlet BC is taken into account. In this way, the FVM solutions are fixed to the prescribed disturbing potential on the upper and side boundaries.

While fixing the lower boundary on the surface of the topography, three upper boundaries are considered at 250 km, 100 km and 10 km, respectively. The FVM approach is used to solve each of them separately. The corresponding solutions, in terms of the disturbing potential T, are compared with the "true" values synthesized directly from EGM2008 to have a rigorous closed-loop check. The root mean squared errors ($T^{FVM} - T^{EGM2008}$), denoted as numerical precisions, as a function of altitudes are shown in Fig. 2.

Figure 2 shows that the numerical precisions of the FVM models can be significantly improved when the upper BC data move closer to the local topography. This is because when the upper boundary is moved closer to the lower boundary, the entire domain size is reduced. The ratio of the number of prescribed boundary conditions to the number of unknowns increases, making the field much easier to determine. However, increasing the discretization beyond

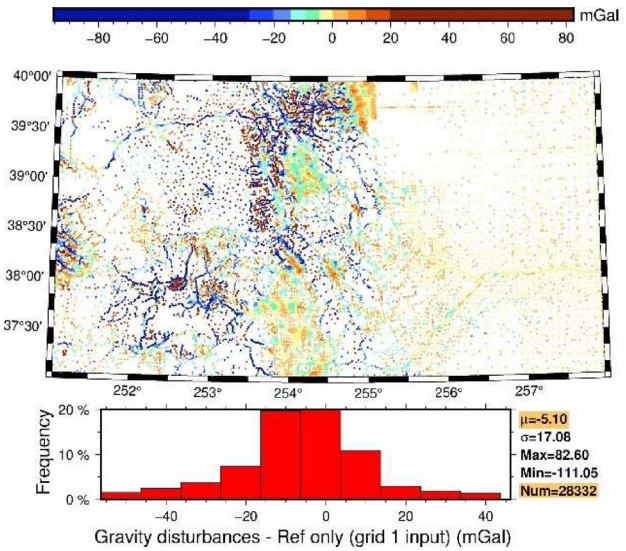

Fig. 5 Residual gravity disturbances after removing the reference field XGeoid22refA (up to d/o 2190) for method 1 (Histogram shows no zero mean and a slightly left skewed tail)

the spatial resolution of the simulated field does not significantly improve the numerical precision. For instance, the synthesized field used here is based on EGM2008, which has a spatial resolution of 5 arc-minutes. Using a denser discretization, such as a 1 arc-min grid, yields numerical results that are identical to those obtained with a 5 arc-min grid, as illustrated by the black dashed curve in Fig. 2. Consequently, the black dashed curve aligns exactly with the red curve in Fig. 2.

4 Real data application

Equation (1) shows that a global gravity anomaly grid is needed in order to determine a geoid model. However, it is impossible to measure gravity everywhere required for

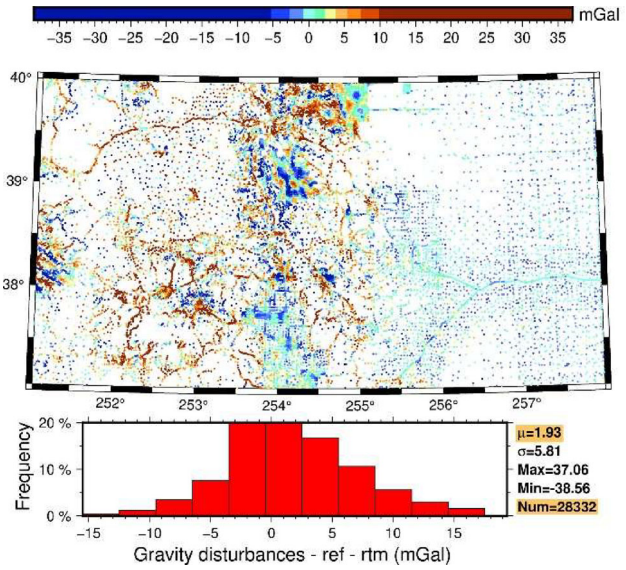

Fig. 6 Residual gravity disturbances after removing the reference field XGeoid22refA (up to d/o 2190) and the RTM effect for method 2 (Histogram shows a near-zero mean-valued normal distribution with a much smaller standard deviation)

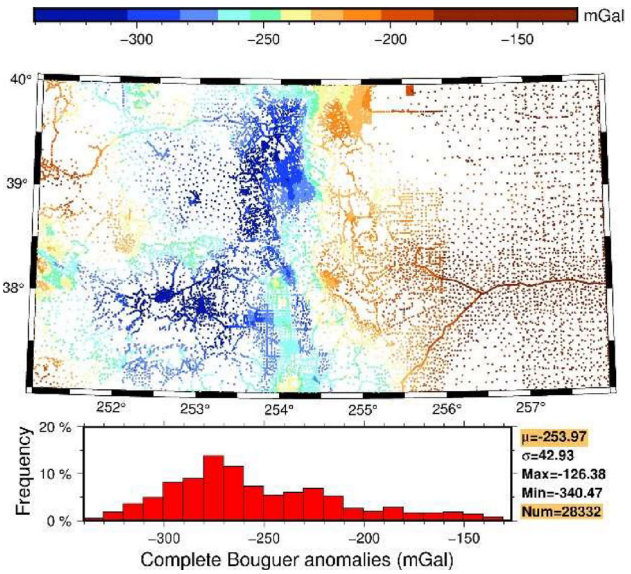

Fig. 7 The complete Bouguer anomalies for method 3 (Histogram does not show a clear normal distribution. And the bias is rather large)

high-resolution geoid determinations. Thus, various satellite missions and airborne campaigns were carried out to provide gravity data coverage. However, please note, they can only make contributions in the middle to low degree part, say n < = 720 in Eq. (1)—the Stokes's kernel has to be modified to best combine them (Li and Wang 2011). Thus, surface gravity data are still very useful in studying the short wavelength features of the local gravity field, specially below 30 km wavelength. In this sense, surface gravity data are indispensable during high-resolution geoid model computation; not further expounded.

4.1 Input gravity data

The Colorado test data published by the National Geodetic Survey, NOAA, USA (Van Westrum et al. 2021; Wang et al. 2021) are used to test the performance of the FVM method. First, the surface dataset is cleaned using the RTM (residual terrain model, Forsberg 1984) residual checking method (Denker et al. 2009; Denker 2015). The essential idea of this method is to use the residual RTM values in a leave-one-out fashion to compare with its neighbor values. If the differences exceed a certain threshold (here an experimentally determined value, 40 mGal, is used), the data are believed to have problems and removed from the dataset. For example, Fig. 3 shows that the 13,740th point (the blue circle in Fig. 3) in the published dataset has over 100 mGal differences compared with the values derived from its nearby observations.

In Fig. 3, about 40 nearby points around the inspection point (the 13,740th point in the published dataset, shown by the blue circle) are used to estimate their RTM residual using LSC with a regularized covariance matrix (Xu 1992; Xu & Rummel 1994). The LSC estimated value, indicated by the green star symbol in Fig. 3, shows over 100 mGal difference to the observed value, which surpassed the threshold of 40 mGal. Thus, this point is removed from the list. This algorithm is applied to all of the datasets to avoid artifacts. Please note that this procedure must be used cautiously due to unbalanced data distributions, i.e., it cannot be fully automatic (Denker 2015). Thus, it is a rather tedious process. The final cleaned data in the target area are shown in Fig. 4 with statistics shown in Table 1.

In principle, the FVM method can work directly with the scattered data. However, it is usually better to grid the data first to ease the programming difficulties. Thus, three different algorithms are tested to grid the scattered points on the idea that a smoother field is easier to make accurate interpolation. Thus, they are all based on the technique of remove–compute–restore. The main differences are on the remove–restore part. The first method only removes a reference model, xGeoid22refA, a spherical harmonic model up to d/o 2190 (Li et al. 2019), without considering the topographic effect explicitly. The second one removes both the reference model and the effect of the RTM (Forsberg 1984) to smooth the residuals further. The last one computes the complete Bouguer anomalies or disturbances for interpolation, which is commonly used in physical geodesy and geophysics, for example, to reconstruct gravity data on the topography, c.f. (Minarechová et al. 2021) or (Čunderlík et al. 2023).

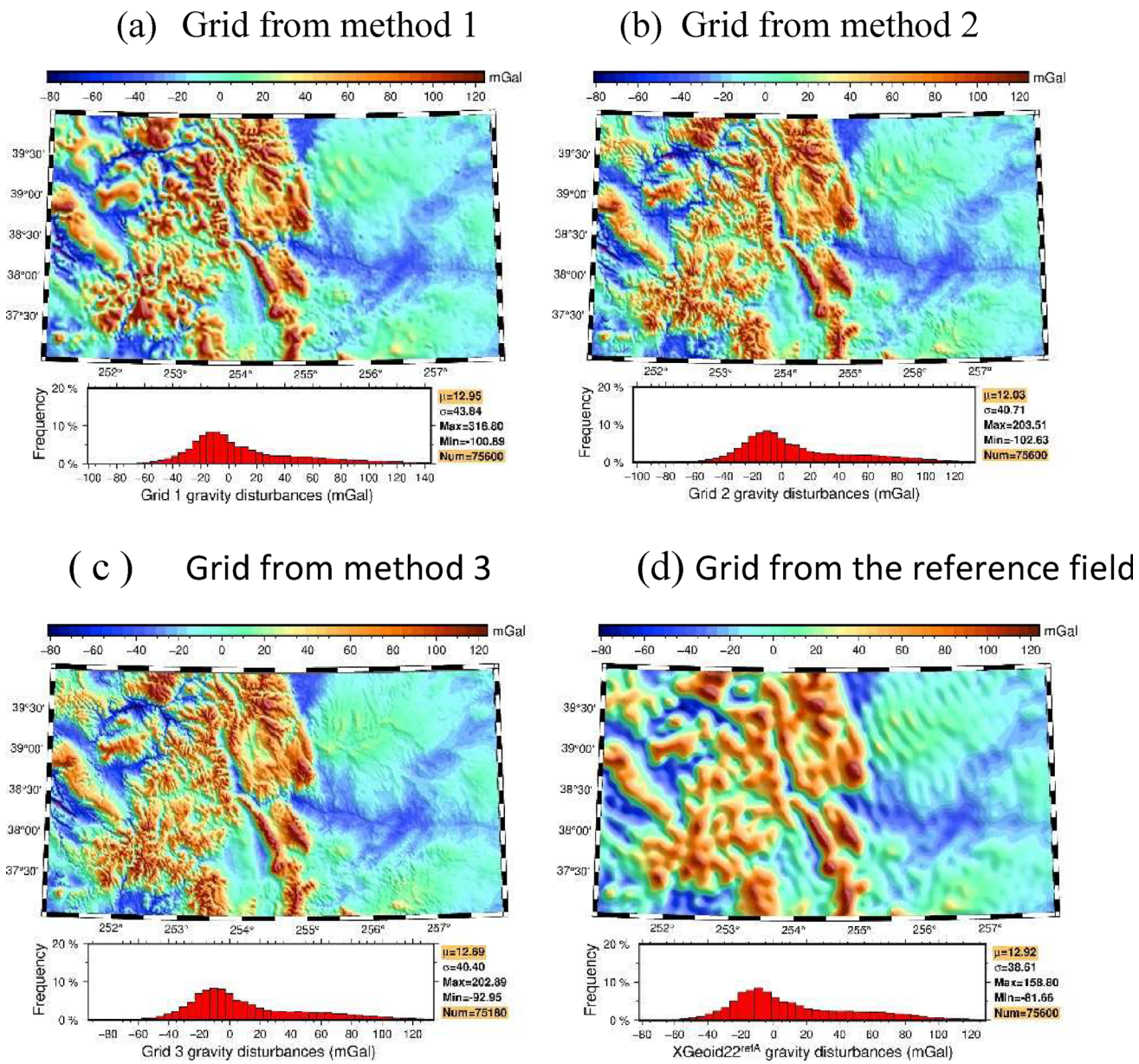

Fig. 8 Gravity disturbance grids from three methods (method 1 upper left (**a**), method 2 upper right (**b**), method 3 lower left (**c**)) and the first estimate synthesized from the reference model (lower right (**d**))

For methods 1 and 2, the cleaned gravity anomalies are first transformed into gravity disturbances using xGeoid22refA geoid values. After removing xGeoid22refA gravity disturbances, the residuals ($\delta g - \delta g^{ref}_{2-2190}$) are shown in Fig. 5. With a mean bias of −5.10 mGal, the residuals also have 17.08 mGal standard deviation, shown in Table 1. For gridding method 1, these residuals are directly used as input without specifically handling the topographical effect. For gridding method 2, the residuals are further smoothed by subtracting the RTM effect (Lin & Li 2022). The final residuals, i.e., $\delta g - \delta g^{ref}_{2-2190} - \delta g^{RTM}$, are shown in Fig. 6 with statistics shown in Table 1. It is clear that after further removing the RTM effects, the residuals are much smoother (standard deviation dropped from 17.08 mGal to 5.81 mGal) and advantageous to interpolation from scattering points to a regular grid. For method 3, the complete Bouguer anomalies, Δg^{CBA}, are first computed using the TopoSK software (Zahorec et al. 2017) and shown in Fig. 7 with statistics shown in Table 1. Afterward, they are transformed to complete Bouguer disturbances. (Remark: In this case, the conventional LSC cannot be used to grid the data, because LSC is based on the ergodic assumption. Apparently, the complete Bouguer gravity disturbances are not ergodic. Thus, the TopoSK software is employed).

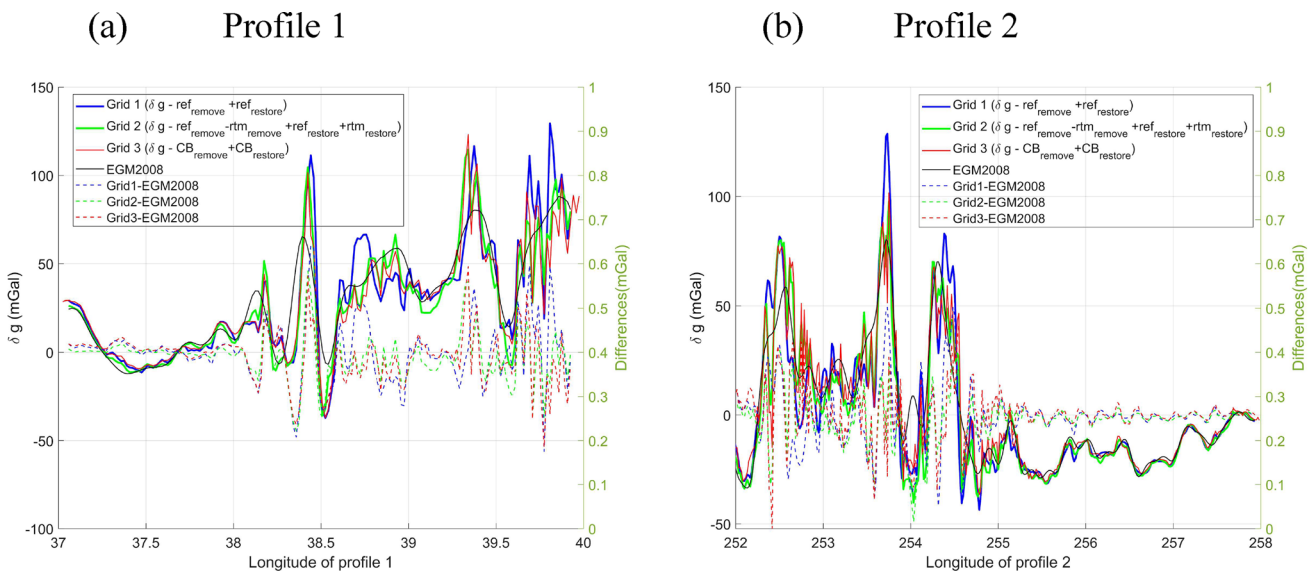

Fig. 9 Two profiles were extracted from Fig. 8. The first one is from north to south along a longitude of 254 degrees (**a**). The other one is from west to east along latitude 38.5 degrees (**b**)

After the removal step, each of the three residual sets is gridded into a regular grid. Then, the corresponding restore step is used to obtain the final gravity disturbance grid on the earth's surface. For method 1, XGeoid22refA is used to synthesize on the grid points and restored; for method 2, both XGeoid22refA and RTM are restored; for method 3, the complete Bouguer effect is restored. Figure 8 shows the gridding results along with the reference grid up to d/o 2190, the preponderance feature of the local gravity field. Two profiles are extracted from the grids to better view the details as well as their differences. The first one is from north to south along a longitude of 254 degrees. The other one is from west to east along latitude 38.5 degrees. The profiles are shown in Fig. 9.

The grids and the extracted profiles shown in Figs. 8 and 9 are similar, figuratively speaking, especially in the flat areas. However, method 1 tends to have more significant omission errors in mountainous regions due to unbalanced data distributions (e.g., from 38.5 to 39 degrees in profile 1). Methods 2 and 3 relieved the problems by forward modeling the terrain effects, and their results are converging.

The published MS05 airborne gravity data are gridded similarly in the mean flight height (Li 2021; Li et al. 2022). These gridded data at altitude of 6000 m are used as the upper BC.

4.2 FVM solutions for different input grids

Together with the lower BCs (three different cases), the FVM approach is applied to solve the local 3D gravity field (a resolution of the 3D computational mesh and computational details are summarized later in Table 2). The disturbing potential obtained on the topography is converted to height anomalies and compared with the GNSS/Leveling data published by Van Westrum et al., (2021). Figure 10 shows the differences between the modeled height anomalies and the observed ones for all three cases, where the bias due to the datum error has been removed for a better view; see Li et al. (2022) for a more detailed discussion.

Through the comparison, we notice that method 2—modeling terrain using the RTM method—yields the best solution for the GNSS/Leveling comparison. The nominally used complete Bouguer method provides similar results.

For completeness, the results from the RTM geoid modeling method—the currently operational geoid computation method (Li et al. 2019)—are also shown in Fig. 10. Compared with the results of this classical method, the FVM results are similar most of time, except from 100 to 150 km in the along-track direction, where the topography profile has a quick elevation change. Overall, the classical method performs about 4 mm better than the FVM method, which is not significant, statistically speaking.

Furthermore, the disturbing potential generated at 230 km from the GO_CONS_GCF_2_DIR_R6 model (DIR6) (Bruinsma et al. 2014) is also used as the upper BC to showcase the benefit of using airborne data in the actual dataset scenario. The corresponding GNSS/Leveling comparison is shown by the black curve in Fig. 10. Unsurprisingly, the precision could not be better than that of the counterparts using airborne data as the upper BCs. Please note, directly using the satellite-only models at 6 km as the upper boundary condition will lead to excruciating errors due to the omission errors in these satellite-only GGM, as shown later in this section.

Table 2 Computational aspects of the FVM solutions for different altitudes of the upper boundary

Altitude of the upper boundary (km)	On the upper boundary fixed to	Mesh size	Spacing (lat × long × height) (m)	Memory coasts (GB)	Total CPU time (h)
230	satellite-only GGM (DIR6)	3196 × 1496 × 1140	0.0033333 × 0.0025 × **200**	522	40.4
100	satellite-only GGM (DIR6)	3196 × 1496 × 980	0.0033333 × 0.0025 × **100**	449	40.9
50	satellite-only GGM (DIR6)	3196 × 1496 × 960	0.0033333 × 0.0025 × **50**	440	31.6
6	airborne gravimetry (GRAV-D)	3196 × 1496 × 800	0.0033333 × 0.0025 × 5	372	19.0

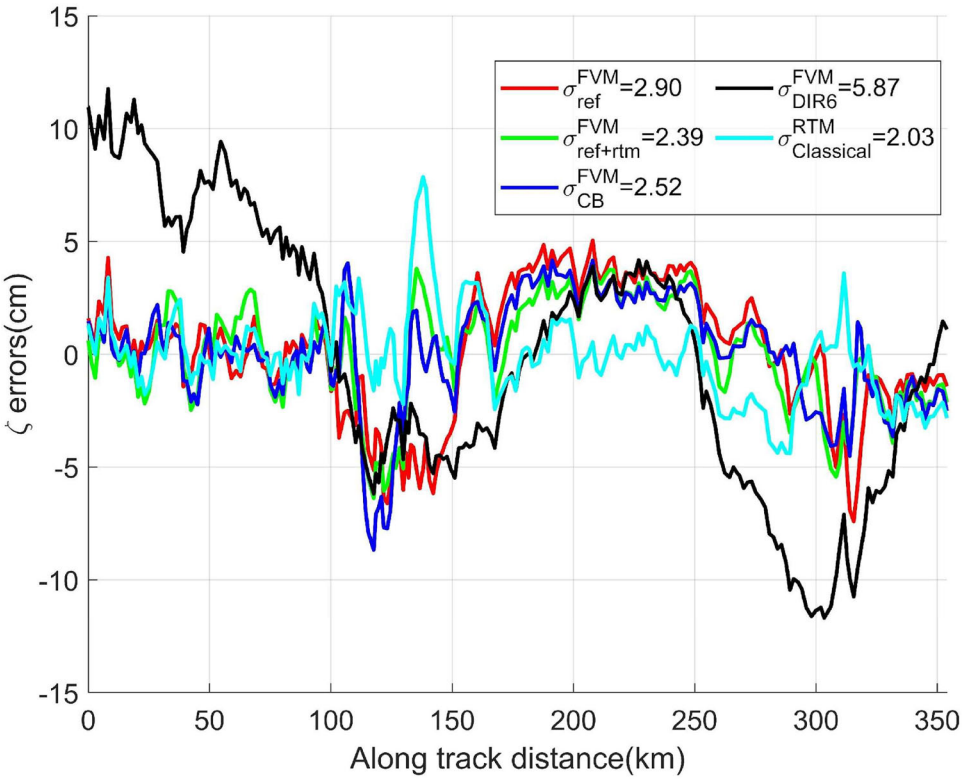

Fig. 10 The height anomalies differences of the FVM models along the GSVS17 route

4.3 Altitude of the upper boundary and its impact on the FVM solutions

The benefit of using airborne data as the upper boundary condition has been demonstrated through simulated and actual data. A natural follow-up question is how to handle areas lacking airborne gravity data. Do we have to set the upper boundary at 250 km on the satellite orbit altitude? Can we use the satellite models directly at 6 km? To answer these questions, we simulated the disturbing potential from EGM2008 (d/o 2190) and EGM2008 (d/o 360) at the same grids on different levels of altitudes, ranging from the topography to the 250 km with steps of 100 m. For example, Fig. 11 shows their differences at 100 km height. Their differences are at mm-level. As such, we propose moving the upper boundary from 250 to 100 km in case no airborne data can be used. Higher than 100 km, the high-resolution models converge to the low-resolution models; see Fig. 11b.

To confirm this finding, we have again performed the numerical experiment with the actual data by lowering the upper boundary from 230 to 100 km and 50 km, respectively. In all cases, the disturbing potential on the upper boundary is generated from the satellite-only model GO_CONS_GCF_2_DIR_R6 up to d/o 300. On the bottom boundary, the surface gravity disturbances from the GRID3 are considered (Fig. 8 lower left). Lowering of the upper boundary allows us to reduce memory costs by the factor 2.3 and 4.6, respectively. However, we have rather decided to decrease a radial size of the finite volumes from 200 m into 100 m and 50 m, respectively, and in this way to reduce the error of the discretization.

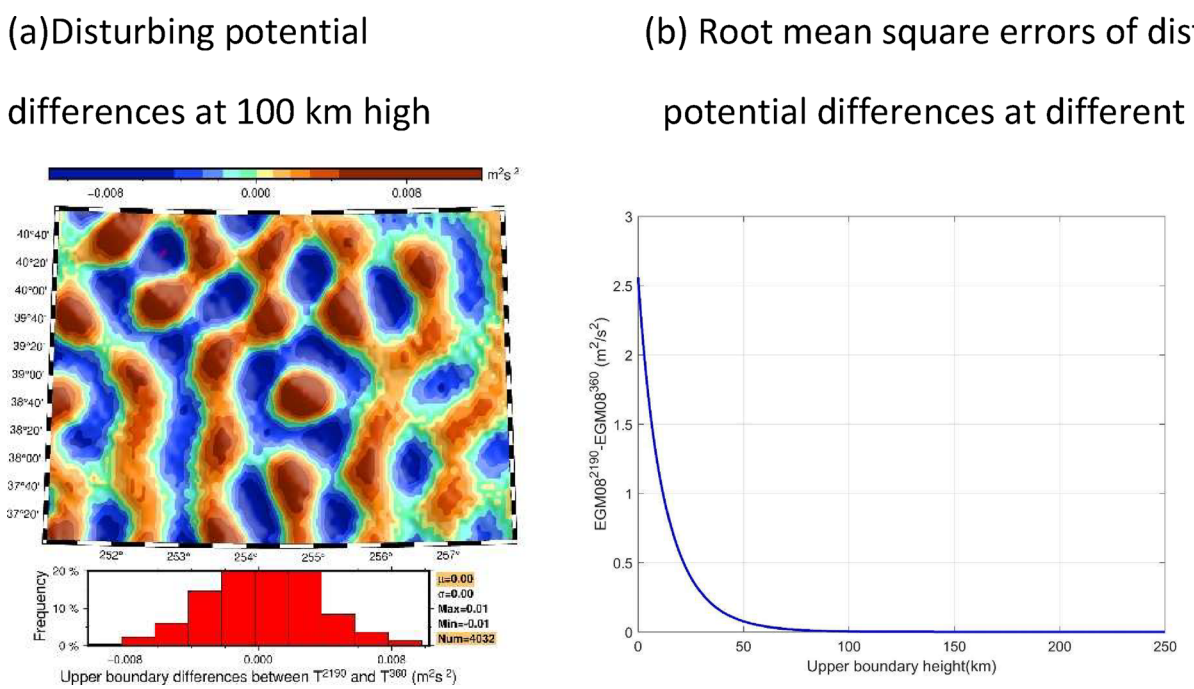

Fig. 11 Disturbing potential differences at 100 km altitude (left (**a**)); disturbing potential differences between low-resolution and high-resolution models at different altitudes (right (**b**))

Table 2 describes computational aspects for all 3 cases as well as for the previous case fixed at 6 km by the airborne gravimetry. Figure 12 depicts differences between the disturbing potential obtained on the topography and one generated from the EIGEN-6C4 model up to d/o 2190 (Förste et al. 2014). It is clear that lowering the upper boundary does help to minimize the differences, especially large negative differences in north-western part (Fig. 12a–c). However, an impact of omission errors starts to increase in case of the upper boundary at 50 km which causes slight 'waves' with amplitudes about 0.5 m^2/s^2 ($\approx$ 5 cm) visible in Fig. 12c. This impact vanishes when using the airborne gravity data as the boundary conditions at altitude of 6 km (Fig. 12d).

However, if the satellite-only GGM is used directly at the airborne altitude, say 6 km, it will cause up to dm-level errors, which is shown in Fig. 13. Thus, due to the well-known omission errors, it is not recommended to directly use the satellite-only models at the airborne flight altitude for high-resolution geoid modeling.

4.4 An extra application in a flat area

Finally, we applied the $FVM_{GRAV\text{-}D}$ approach to the GSVS11 area, which is a rather flat area located in Southern Texas. The height anomaly comparison at the GNSS/Leveling benchmarks, provided by Smith et al. (2013), is shown in Fig. 14. Compared with the counterparts from the RTM geoid modeling approach (Li et al. 2019), the results are very similar, only 2 mm (well within the GNSS/Leveling error budget) differences in the standard deviations. Through these comparisons, we conclude that the FVM approach provides an efficient numerical option to utilize airborne gravity data for local gravity field computation without heavy regularizations or complicated spectrum manipulations that are common routines needed in classical methods.

5 Discussion

The results presented in this study underscore the significant advancements made in addressing the GBVP using FVM, particularly in the context of airborne gravity data. Our findings demonstrate that strategically lowering the upper boundary condition (BC) to 10 km or even 100 km enhances the precision of geoid modeling while also reducing computational demands. This is particularly relevant as we navigate the challenges posed by the downward continuation problem, traditionally exacerbated by the radial ratio term in classical methods.

The comparative analysis between the FVM approach and classical techniques reveals several critical insights. First, the simulation results indicate a clear advantage in numerical precision when the upper boundary is brought closer to the local topography. The relationship between the position of the upper BC and the number of prescribed boundary conditions is pivotal; as the upper BC is lowered, the volume

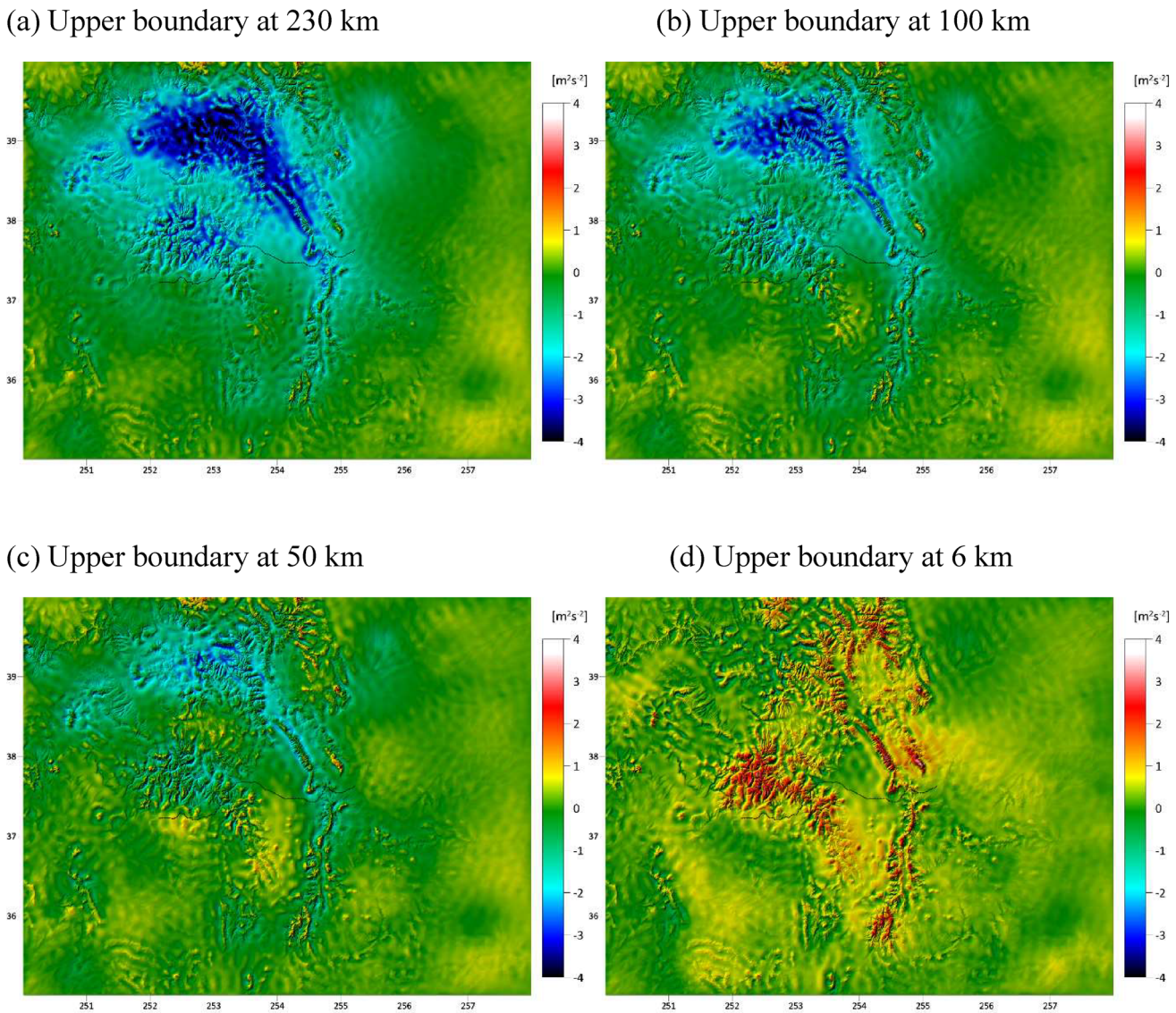

Fig. 12 Differences between the obtained disturbing potential on the topography and EIGEN-6C4 for different altitude of the upper boundary **a** 230 km, **b** 100 km, **c** 50 km and **d** 6 km (fixed by airborne gravimetry)

of the computational domain decreases, increasing the ratio of known boundary conditions to unknowns. This change significantly simplifies the problem, leading to improved convergence and accuracy in the final models.

Furthermore, the application of the FVM approach to real datasets, particularly in challenging topographies like Colorado, reinforces its robustness. The results highlight how traditional methods may struggle with unbalanced data distributions in mountainous regions, leading to potential omission errors. Our findings suggest that utilizing RTM to mitigate these effects is beneficial, with the RTM approach yielding comparable results to the complete Bouguer method. This convergence is reassuring, as it suggests that both methods can effectively model local gravity fields, albeit with different underlying assumptions and approaches.

Another crucial aspect is the careful data quality checks applied throughout our study. The rigorous cleaning of the gravity data using residual terrain models is essential in ensuring that the final models accurately reflect the local gravity field. This tedious but necessary process exemplifies the commitment to data integrity.

As we consider areas lacking airborne data, our study's findings encourage a reevaluation of the upper BC placement. Lowering the upper BC to 100 km appears to be a feasible compromise, preserving accuracy while addressing computational constraints. The simulations demonstrate that at this altitude, the convergence of high-resolution models to lower-resolution models can be achieved without substantial precision loss, thus providing a viable pathway for geoid modeling in airborne free regions.

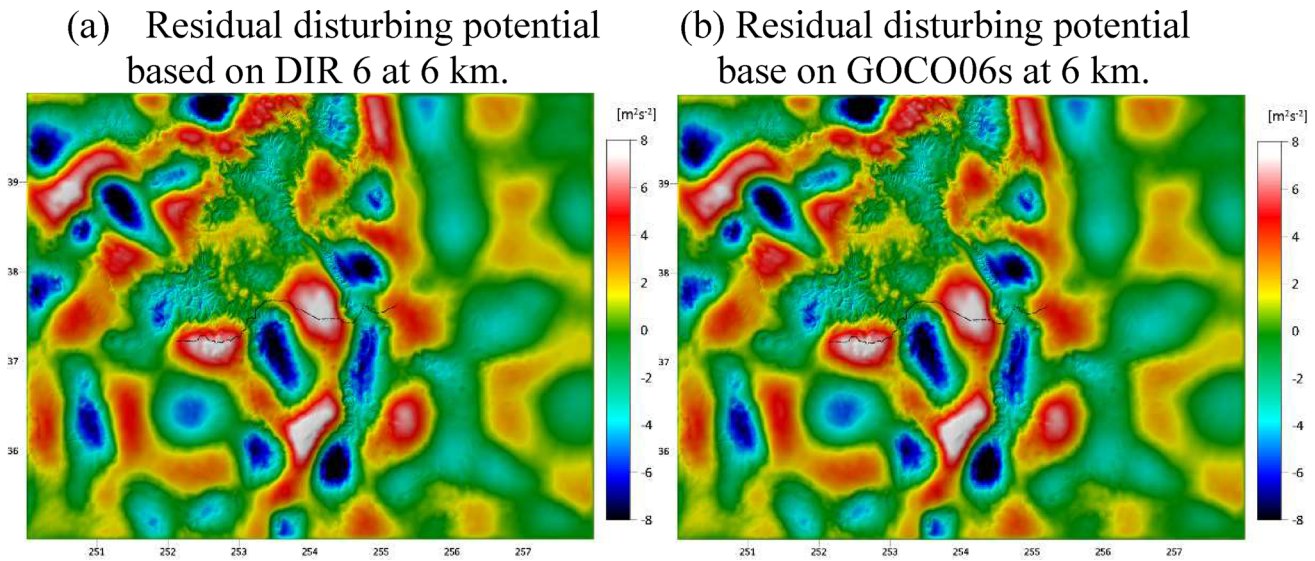

Fig. 13 Differences between the obtained disturbing potential on the topography and EIGEN-6C4 when fixing the upper boundary at 6 km by directly using DIR6 (left (**a**)) or GOCO06s (right (**b**)) (Kvas et al. 2021)

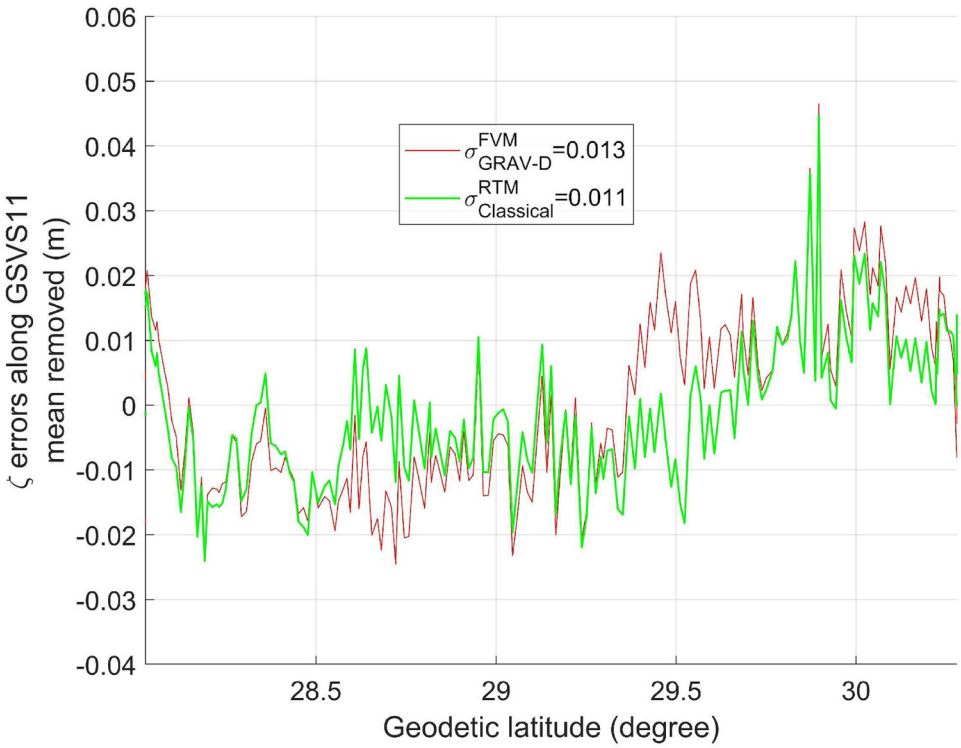

Fig. 14 Height anomaly errors at the GSVS11 benchmarks from both the $FVM_{GRAV\text{-}D}$ approach and the classical RTM geoid modeling method

In conclusion, the FVM approach presents a powerful alternative for solving the GBVP in physical geodesy, particularly with the increasing availability of airborne gravity data. The integration of this method offers not only improved precision in local gravity field computations but also a reduction in the computational burdens. Future research may explore further enhancements to the FVM framework, including adaptive meshing techniques and optimization algorithms, to continue refining geoid modeling efforts in diverse geophysical contexts.

6 Summary

Analytical methodologies for addressing GBVPs in physical geodesy, particularly those encountering the inevitable

downward continuation problem, are essential, as evidenced by the radial ratio term being exponentially magnified by the spherical harmonic degree. FVM provides a numerical tool to solve GBVPs without specifically handling this irritating radial-related term. Given that all the U.S. are covered with uniformly distributed airborne gravity data, this creates an ideal scenario for applying the FVM approach. This is especially true in the study area with relatively good surface gravity data, as the recently successful Colorado experiment proved. The much-lowered upper BC provided by the airborne data also significantly relieved its peevish computation costs. Both simulated data and actual data demonstrate the precision improvements by lowering the upper BC from the satellite altitude to the flight level of the airborne gravimetry. A holistic data quality check is applied to every surface gravity observation to ensure their authenticity in representing the local gravity field, albeit it is a rather tedious process. Three removal strategies are applied to mitigate the omission errors caused by unbalanced data distributions in the surface data. Numerical tests show that both the RTM approach and the complete Bouguer method yield similar results. For areas without airborne gravimetry coverage, numerical tests show that lowering the upper BC to 100 km will not significantly decrease the precision if saving computation cost is a must.

Acknowledgements The work of RC, MM and ZM was supported by the Grant VEGA 1/0690/24 and projects APVV-19-0460 and APVV-23-0186. The work of PZ and JP was supported by the Grant VEGA 1/0587/24. The authors really appreciate all the constructive comments given by the three reviewers and editors who un-conservatively shared their wisdoms with us.

References

Bruinsma S, Förste C, Abrikosov O, Lemoine J, Marty J, Mulet S, Rio M, Bonvalot S (2014) ESA's satellite-only gravity field model via the direct approach based on all GOCE data. Geophys Res Lett 41(21):7508–7514. https://doi.org/10.1002/2014GL062045

Childers VA, Bell RE, Brozena JM (1999) Airborne gravimetry; an investigation of filtering. Geophysics 64:61–69

Čunderlík R, Medla M, Mikula K (2020) Local quasigeoid modeling in Slovakia using the finite volume method on the discretized Earth's topography. Contrib Geophys Geod 50(3):287–302. https://doi.org/10.31577/congeo.2020.50.3.1

Čunderlík R, Tenzer R, Macák M, Zahorec P, Papčo J, Nsiah Ababio A (2023) A detailed quasigeoid model of the Hong Kong territories computed by applying a finite-element method of solving the oblique derivative boundary-value problem. J Geod Sci 13(1):20220153. https://doi.org/10.1515/jogs-2022-0153

Čunderlík R, Macák M, Kollár M, Minarechová Z, Mikula K (2024) 3D high-resolution numerical modeling of altimetry-derived marine gravity data. J Geodesy (submitted in July 2023)

Denker H et al (2009) The development of the European gravimetric geoid model EGG07. In: Sideris MG (ed) Observing our changing earth. International Association of Geodesy Symposia, vol 133. Springer, Berlin, pp 177–185. https://doi.org/10.1007/978-3-540-85426-5_21

Denker H (2015) A new European gravimetric (quasi)geoid EGG2015. In: Poster presented at XXVI general assembly of the international union of geodesy and geophysics (IUGG), earth and environmental sciences for future generations, 22 June–02 July 2015. Czech Republic: Prague

Eymard R, Gallouët T, Herbin R (2000) Finite volume methods. In: Handbook for numerical analysis, vol 7. Elsevier, Amsterdam, pp 713–1020

Fašková Z, Čunderlík R, Mikula K (2010) Finite element method for solving geodetic boundary value problems. J Geod 84:135–144

Forsberg R, Olesen AV, Keller K, Møller M (2001) Airborne gravity and geoid surveys in the Arctic and Baltic seas. In: Proceedings of international symposium on kinematic systems in geodesy, geomatics and navigation. Banff, Canada, pp 586–593

Forsberg R (1984) A study of terrain reductions, density anomalies and geophysical inversion methods in gravity field modeling. In: OSU report 355, Ohio State University, Columbus, Department Of Geodetic Science and Surveying

Förste C, Bruinsma SL, Abrikosov O, Lemoine JM, Marty JC, Flechtner F, Balmino G, Barthelmes F, Biancale R (2014) EIGEN6C4 The latest combined global gravity field model including GOCE data up to degree and order 2190 of GFZ Potsdam and GRGS Toulouse. GFZ Data Services

Heiskanen WA, Moritz H (1967) Physical geodesy. Freeman & Comp, San Francisco

Huang J, Véronneau M (2013) Canadian gravimetric geoid model 2010. J Geod 87:771–790. https://doi.org/10.1007/s00190-013-0645-0

Klees R, Tenzer R, Prutkin I, Wittwer T (2008) A data-driven approach to local gravity field modeling using spherical radial basis functions. J Geod 82:457–471. https://doi.org/10.1007/s00190-007-0196-3

Kvas A, Brockmann JM, Krauss S, Schubert T, Gruber T, Meyer U, Mayer-Gürr T, Schuh WD, Jäggi A, Pail R (2021) GOCO06s: a satellite-only global gravity field model. Earth Syst Sci Data 13(1):99–118. https://doi.org/10.5194/essd-13-99-2021

Li X (2011) Strapdown INS/DGPS airborne gravimetry tests in the Gulf of Mexico. J Geod 85:597–605

Li X (2018a) Modeling the North American vertical datum of 1988 errors in the conterminous United States. J Geod Sci 8(1):1–13

Li X (2018b) Using radial basis functions in airborne gravimetry for local geoid improvement. J Geod 92:471–485

Li X (2021) Leveling airborne and surface gravity surveys. Appl Geomat 13:945–951. https://doi.org/10.1007/s12518-021-00402-2

Li X, Wang Y-M (2011) Comparisons of geoid models over Alaska computed with different Stokes's kernel modifications. J Geod Sci 1(2):136–142. https://doi.org/10.2478/v10156-010-0016-1

Li X, Crowley JW, Holmes SA, Wang YM (2016) The contribution of the GRAV-D airborne gravity to geoid determination in the Great Lakes region. Geophys Res Lett 43:4358–4365

Li X, Huang J, Klees R et al (2022) Characterization and stabilization of the downward continuation problem for airborne gravity data. J Geod. https://doi.org/10.1007/s00190-022-01607-y

Li X, Ahlgren K, Hardy R, Krcmaric J, Wang Y (2019) The development and evaluation of the experimental gravimetric geoid model 2019. https://beta.ngs.noaa.gov/GEOID/xGEOID19/xGeoid19_tech_details.v10.pdf

Lin M, Li X (2022) Impacts of using the rigorous topographic gravity modeling method and lateral density variation model on topographic reductions and geoid modeling: a case study in Colorado, USA. Surv Geophys 43:1497–1538

Macák M, Čunderlík R, Mikula K, Minarechová Z (2021) Computational optimization in solving the geodetic boundary value problems. Discrete Continuous Dyn Syst 14(3):987–999. https://doi.org/10.3934/dcdss.2020381

Minarechová Z, Macák M, Čunderlík R, Mikula K (2015) High-resolution global gravity field modeling by the finite volume method. Stud Geophys Geod 59:1–20

Minarechová Z, Macák M, Čunderlík R et al (2021) On the finite element method for solving the oblique derivative boundary value problems and its application in local gravity field modeling. J Geod. https://doi.org/10.1007/s00190-021-01522-8

Moritz H (1980) Advanced physical geodesy. H. Wichmann Verlag, Karlsruhe

Pavlis NK, Holmes SA, Kenyon S, Factor JK (2012) The development and evaluation of the earth gravitational model 2008 (EGM2008). J Geophys Res Solid Earth 117(B4):B04406

Reddy JN (2006) An introduction to the finite element method, 3rd edn. McGraw-Hill Education, New York

Schmidt M, Fengler M, Mayer-Guerr T, Eicker A, Kusche J, Sanchez L, Han SC (2007) Regional gravity field modeling in terms of spherical base functions. J Geod 81(1):17–38. https://doi.org/10.1007/s00190-006-0101-5

Sjöberg LE, Abrehdary M (2023) Geoid or quasi-geoid? A short comparison. In: International association of geodesy symposia. Springer, Berlin. https://doi.org/10.1007/1345_2023_199

Smith DA, Holmes SA, Li X, Guillaume Y, Wang YM, Brki B, Roman DR, Damiani TM (2013) Confirming regional 1 cm differential geoid accuracy from airborne gravimetry: the Geoid Slope Validation Survey of 2011. J Geod 87(1012):885–907. https://doi.org/10.1007/s00190-013-0653-0

Tscherning CC, Rapp RH (1974) Closed covariance expressions for gravity anomalies, geoid undulations, and deflections of the vertical implied by anomaly degree-variance models. In: Reports of the department of geodetic science No. 208. The Ohio State University, Columbus

Wang Y, Sánchez L, Ågren J, Huang J, Forsberg R, Abd-Elmotaal HA, Ahlgren K, Barzaghi R, Bašić T, Carrion D, Claessens S, Erol B, Erol S, Filmer M, Grigoriadis VN, Isik MS, Jiang T, Koç Ö, Krcmaric J, Li X, Liu Q, Matsuo K, Natsiopoulos DA, Novák P, Pail R, Pitoňák M, Schmidt M, Varga M, Vergos GS, Véronneau M, Willberg M, Zingerle P (2021) Colorado geoid computation experiment: overview and summary. J Geod 95(12):1–21

Van Westrum, D, Ahlgren K, Hirt C et al (2021) A geoid slope validation survey (2017) in the rugged terrain of Colorado, USA. J Geodesy 95(9)

Xu P (1992) Determination of surface gravity anomalies using gradiometric observables. Geophys J Int 110:321–332

Xu P, Rummel R (1994) Generalized ridge regression with applications in determination of potential fields. Manuscr Geodaet 20:8–20

Zahorec P, Marušiak I, Mikuška J, Pašteka R, Papčo J (2017) Numerical calculation of terrain correction within the Bouguer anomaly evaluation (Program TopoSK), (Chapter 5). In: Pašteka R, Mikuška J, Meurers B (eds) Understanding the Bouguer anomaly: a gravimetry puzzle. Elsevier, Amsterdam, pp 79–92